Landslides (2022) 19:2439–2458
DOI 10.1007/s10346-022-01926-3
Received: 14 November 2021
Accepted: 16 June 2022
Published online: 24 June 2022

Shu-wei Sun · Liu Liu · Jia-bing Hu · Hui Ding

Failure characteristics and mechanism of a rain-triggered landslide in the northern longwall of Fushun west open pit, China

Abstract A rainfall-induced landslide occurred in the north highwall of the Fushun west open pit at 5:00 (UTC + 8) on July 26, 2016, in China. The landslide was about 3.1×10^6 m^3 and caused considerable destruction of houses, roads, and railways. Field investigations, laboratory tests, and numerical analyses have been performed to explore the failure characteristics and formation mechanism of the landslide. The landslide was divided into three parts: the crack area, the sliding body area, and the accumulation area. The X-ray diffraction and scanning electron microscope techniques were used to reveal the mineral composition and microstructure of the landslide material. Then, a conceptual model of the landslide mechanism was constructed and the process of the landslide was divided into four stages: unloading and cracking stage; sliding and partial locking stage; shearing out and failure stage; and flowing and accumulating stage. A combined seepage and stability analysis was performed to explore the mechanism of the landslide by numerical simulation. The relationship of volumetric water content and hydraulic conductivity to matric suction was established to describe the hydraulic characteristics of the slope material under infiltration. The results show that the maximum matric suction in the slope decreases continually with the increase of rainfall intensity and duration, and the north highwall will not be stable after 7.2 h for 16 mm/h of rainfall. The original slope was stable and heavy rainfall triggered the landslide, and the obtained critical failure surface matched the field survey closely. The findings improved understanding of the failure mechanism and process of rainfall-induced landslides may be used for evaluating the stability of slopes and early identification for both active and inactive open-pit mines.

Keywords Rainfall-induced landslides · Open-pit slope · Fushun west opencast · Failure mechanism · Transient seepage analysis · Slope stability analysis

Introduction

Rainfall-induced landslides are common geological hazards that cause a large number of casualties and heavy economic losses around the world. For instance, in 2013, the heavy rainfall triggered 708 loess landslides in Tianshui City, which killed 24 people and caused the collapse of 2386 houses (Zhang et al. 2016). In 2016, a rock avalanche triggered by intense and continuous rainfall suddenly collapsed and rushed down towards the houses in Su village, which buried more than 20 houses and caused 27 deaths (Ouyang et al. 2018). On June 24, 2017, a catastrophic rock avalanche destroyed the whole village in Xinmo and led to about 10 deaths, which was induced by long-term and high-intensity rainfall (Fan et al. 2017). Such landslides draw much attention not only because damage such as large-scale collapse can cause severe loss of life and property, but also because of difficulties in understanding the mechanism of instability evolution under rainfall infiltration (Nguyen et al. 2020). Therefore, it is important to deeply investigate the failure characteristics and mechanism of slopes under rainfall conditions.

In recent decades, the influence of rainwater on the behavior of slopes has been widely studied based on field investigations, laboratory tests, numerical analyses, and model tests (Rahardjo et al. 1995; Zhang et al. 2011; Sun et al. 2021). Numerous studies have demonstrated that the infiltration of rainwater significantly decreased the stability level of slopes because rainwater not only increases the unit weight and water content of slopes, but also changes the pore-water pressure and reduces the shear strength (Chen et al. 2020). Besides, an increase in water content of discontinuities causes a significant decrease in rock mass stiffness, and the water-induced weakening effect may have a more significant influence on rock mass slope stability (Ren et al. 2020). A series of parametric studies have been performed to investigate the effect of various factors affecting rainfall-induced landslides, such as rainfall intensity, rainfall duration, and antecedent rainfall (Cai and Ugai 2004; Raj and Sengupta 2014). However, studies on specific failure mechanisms of infiltrated slopes are still limited since the rainwater infiltration and landslide initiation are a complex process.

Different methods have been used to reconstruct and analyze the slope seepage and stability under rainfall infiltration, which contributes to a better understanding of driving mechanism and failure process of landslides (Lu et al. 2013; Zhan et al. 2019). Leshchinsky et al. (2015) applied transient unsaturated seepage-stress finite element analysis to investigate the complex behaviors of a progressive slope failure in Yumokjeong, Korea. Wu et al. (2016) developed an analytical approach for rainfall infiltration in an unsaturated porous medium, including an analytical solution for the factor of safety of an infinite partially saturated slope. Yang et al. (2017) coupled finite element analysis and unsaturated seepage concept to investigate the failure and deformation mechanism of slopes in Taipei City, Taiwan Province. These studies have demonstrated that the variation of the seepage field in a slope is significantly affected by rainfall patterns, hydraulic conductivity, and groundwater conditions, which control the flux condition and affect the fluid flow, thereby changing the stable state of the slope. Coupling rainfall seepage with slope stability analysis is advantageous for understanding the mechanism of rainfall-triggered landslides (Chung et al. 2017; Chen et al. 2021). Hence, it is essential to carry out coupled seepage and stability analysis of the slope under various rainfall conditions to provide an insight into the mechanism

of rainfall-induced landslides and the controlling factors of slope instability.

This study explores the failure characteristics and formation mechanism of a rainfall-induced landslide at the Fushun west open pit. Field investigations, laboratory tests, and numerical analyses are carried out in detail. A simplified coupled seepage and stability analysis where the pore-water pressures obtained from the transient seepage analysis are included in the limit equilibrium analysis is performed to explore the mechanism of the landslide by numerical simulation. The pore-water pressure and stability of the slope under different rainfall intensities and duration are examined during the analysis. The findings from this study may improve understanding of the failure mechanism and process of rainfall-induced landslides, and can also be used to evaluate slope stability and early identification for both active and inactive open-pit mines.

Condition of the landslide

Study area

The Fushun west opencast mine is a large open-pit coal mine in western Fushun, 60 km to Shenyang (Fig. 1a). The site has a long mining history of more than 100 years and is the largest open pit in Asia (Nie et al. 2015). Its length from east to west is 6.6 km, and it has a width of 2.2 km from north to south with a maximum depth of approximately 420 m (Fig. 1b). The main products are residual coal and oil shale. By the end of 2019, more than 280 Mt of coal and 530 Mt of oil shale had been produced. In the meantime, landslide hazards caused by more than 100 years of opencast mining have brought the city increasingly severe environmental and geological problems.

Landslide events

The landslide in Fushun west open pit is characterized by wide distribution, long duration, and high-intensity damage. Based on historical landslide data (Fig. 2), over 100 landslide events occurred in the open pit, with 29 recorded on the north highwall. For example, in April 1979, a green mudstone landslide occurred due to the long-term erosion of rainwater, which was the first landslide on the north highwall of the pit, with a total volume of about 5.0×10^4 m^3 (Gao 2017). In August 1993, the Fushun area experienced a rainstorm with accumulated daily rainfall exceeding 200 mm, which caused a large-scale deformation and a landslide in the north highwall, and the volume of the sliding body exceeded 4.5×10^6 m^3 (Cui 2018). In July 2015, under the combined action of mining activity and rainfall infiltration, a green mudstone landslide occurred in the lower part of the north highwall, and the volume of sliding mass was estimated to be 6.9×10^5 m^3 (Li et al. 2015). These landslides were mainly triggered by seasonal rainfall, occurred within a short period of time, and caused severe damage to buildings, underground pipelines, roads, and railways. Characterizing the failure mechanism and process of this type of landslide may help evaluate the stability of open pit slopes in both active and inactive mines, thus providing warning signs to aid the early identification of landslides.

At 5:00 (UTC + 8) on July 26, 2016, a large landslide (N 41°51′3.39″, E 123°52′58.31″) occurred in the north highwall of the Fushun west open pit owing to the heavy rainfall, and its location is in the middle of the highwall (Fig. 2). The main sliding direction of the landslide is approximately SE 6° inside the open pit. The length of the slide in the sliding direction is about 350 m, and the maximum width from east to west is about 500 m. The landslide destroyed 40 houses of 25 families and damaged 20 houses, which caused the evacuation of 1026 people. The volume of the landslide body is estimated to be 3.1×10^6 m^3 based on the difference between the pre- and post-sliding digital elevation models (DEMs) of the landslide area. The direct economic loss is approximately RMB 17.82 million due to the combined damage to roads, railroads, equipment, and buildings.

Characteristics of the landslide

To obtain the failure characteristics of the landslide, field investigation and DEM data were analyzed. Figure 3 shows the elevation variations of the slope profile a-a' before and after the landslide (section location shown in Fig. 2), and it can be seen that the landslide area is located on the upper part of the slope and the rear of the landslide is close to downtown Fushun. The sliding surface marked by a red dash line presents a near arc shape, and it is noted that the sliding surface is partly exposed to saturated conditions (below the water table). There are several roads and railways that run through the landslide area, among which Yongshou and Xingping are urban roads located at the crest of the slope, and R#2, R#4, R#9, R#12, R#14, and R#17 are the railways for the transportation of oil shale and waste materials located at the bench of the slope (Fig. 4a). After the event, the landslide area presents a tongue-shaped topography in plain view (Fig. 4b). The body slid down the slope, and buried and damaged the transport railways and urban roads, which seriously affected the normal operation of the mine and the safety of residents. According to the failure characteristics of the landslide, the landslide area is divided into three parts: the crack area (I), the sliding body area (II), and the accumulation area (III).

The crack area (I)

The crack area (I) is located at the top of the slope at an elevation of 75 m a.s.l. (Fig. 3). The area is about 500-m long from east to west and distributed with many arc opening cracks. The main scarp of the landslide is located at the slope crest (Fig. 5a), which presents a near-vertical and conspicuous recliner-like shape with an elevation of 50–75 m a.s.l. and up to 25 m high. The main compositions of the exposed scarp include loose surface clay and gravel. The crack area was mainly formed by traction unloading of the landslide, and its failure was characterized by the development of numerous transverse tensile cracks and significant downhill displacement. The expanded cracks severely damaged the constructions and roads, and many unstable blocks remain perched on the crack area (Fig. 5b).

The sliding body area (II)

The part is the main sliding area about 350 m in length and 500 m in width, consisting mainly of weathered mudstone and few surface clays. The trailing and leading edges of the sliding body are at 75 m and − 18 m a.s.l., respectively. It can be seen

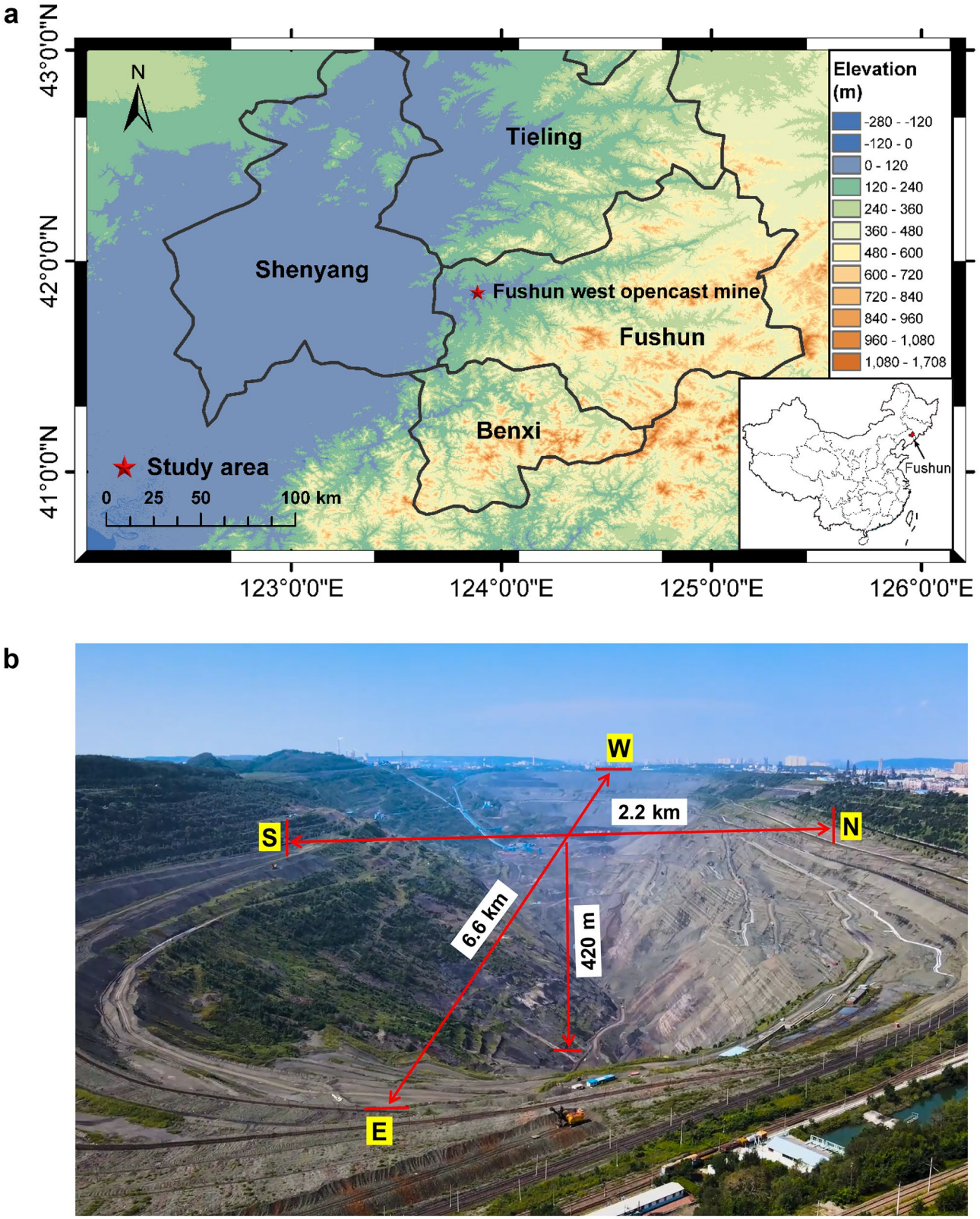

Fig. 1 Study area location. **a** Location of the open pit in Fushun City, China, **b** photo of the Fushun west open pit

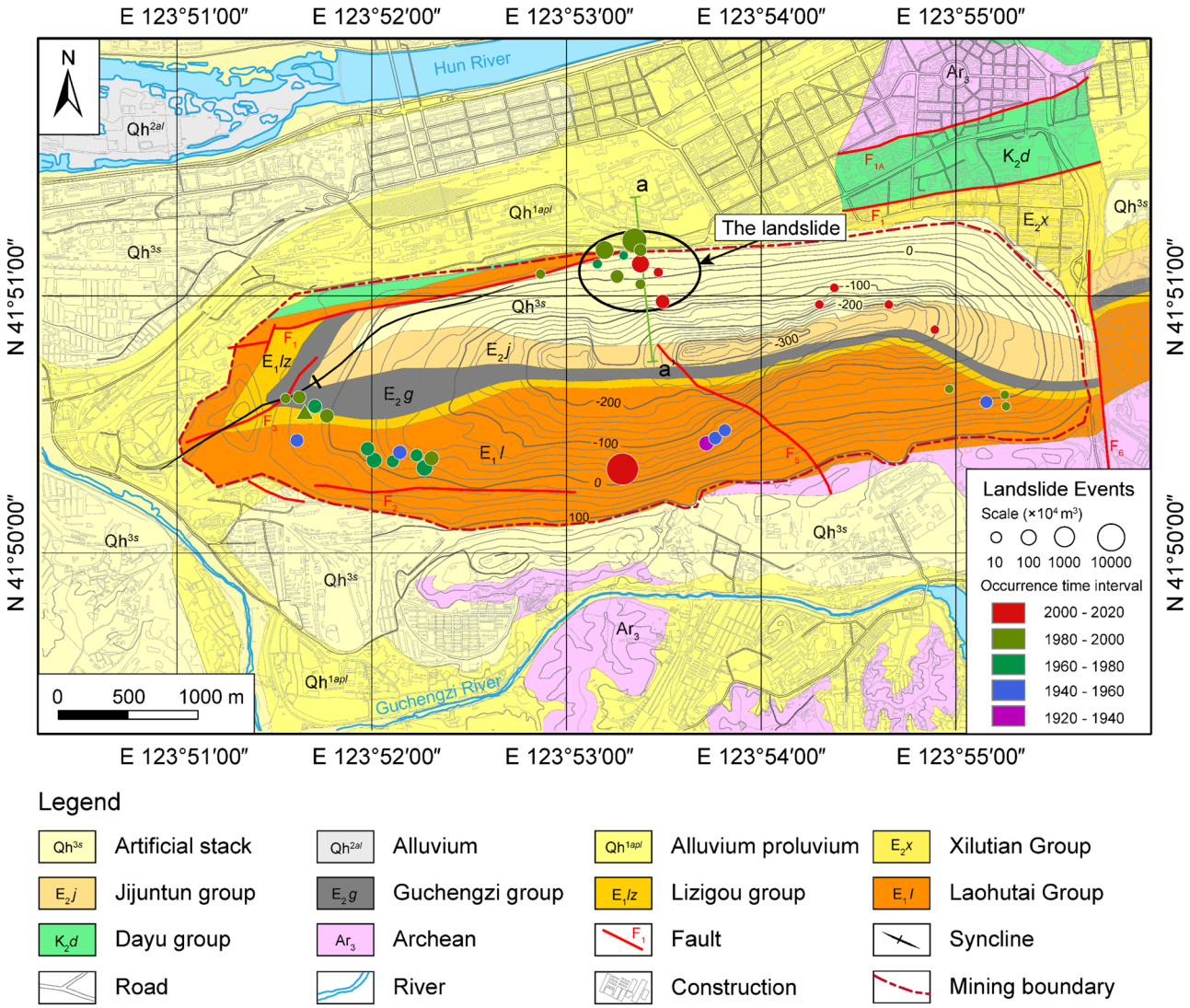

Fig. 2 Engineering geological map of study area and location of the landslide

from Fig. 6a that the sliding body slid down the main scarp, which caused severe damage to the railway R #2 and constructions at the trailing edge of the landslide. In addition, after the slide, a platform was formed by relative shear deformation. The typical feature of this platform is basically intact vegetation, indicating that the sliding mass kept relatively good integrity. Figure 6b shows the shear outlet of the landslide at the front part of the sliding body. Under the pushing action of the sliding mass, the railway R #12 was destroyed, while the trees, houses, and wire poles were tilted backward. These features reflect the rotational failure mode occurring at the landslide toe. This typical sliding is characterized by a prominent main scarp, arc-shaped sliding surface, slow or moderate velocities, and limited internal deformation. Examples of this failure type include the Montepiano landslide (Hungr et al. 2014), the Stogovce landslide (Jemec Auflič et al. 2017), and the Thong Nhat landslide (Nguyen et al. 2020).

The accumulation area (III)

The landslide debris moved downstream and formed an accumulation area along the slope. Controlled by the shape of the slope, several parts of the accumulation mass were situated on the benches, while others were deposited at the pit bottom. The accumulation mass on the benches was formed by the collapse of the leading edge of the sliding body, which blocked the mining transport roads and railways (Fig. 6c). The landslide debris consists mainly of broken green mudstone with unclear edges and corners. Combined with the geological characteristics of the area before the sliding, the bottom accumulation originated from the disintegration and fragmentation of the upper rock mass with a maximum movement distance of 600 m. Besides, we found that the accumulation mass showed evidence of a previous landslide, as rock mass disintegrates and tension cracks could be observed on the slope surface.

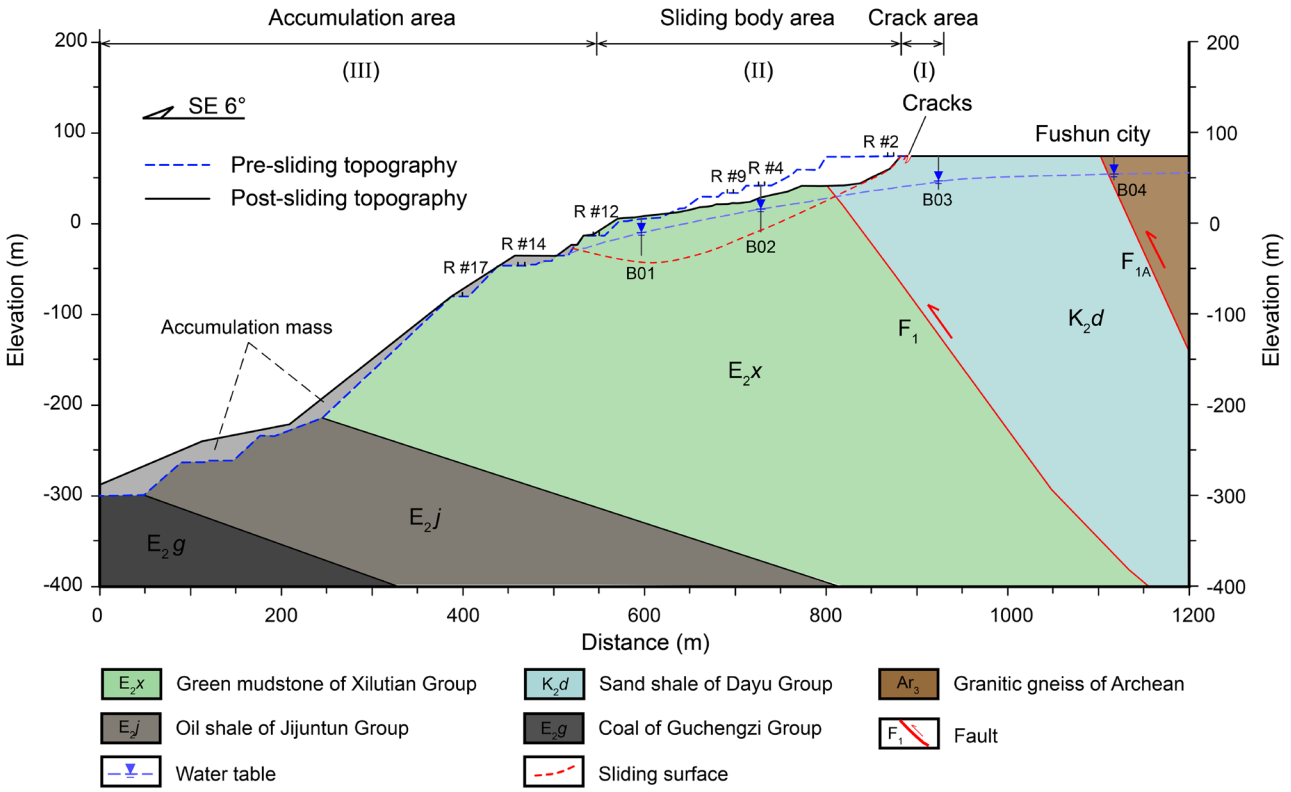

Fig. 3 Slope elevation variations from before and after the landslide of profile a-a′

Geological characteristics of the landslide area

The lithology of the landslide area was studied by means of drilling and field surveys. Borehole investigations revealed that the strata mainly consist of the Xilutian Group (E_2x), Jijuntun Group (E_2j), Guchengzi Group (E_2g), Dayu Group (K_2d), and Archean (Ar_3) (Fig. 3). The uppermost layer is the loose surface clay and gravels originating from the in-place weathered bedrock with a thickness of 5 to 24.3 m, and some of them had been removed during mining activity. The main exposed layers are green mudstone of Xilutian Group (E_2x), oil shale of Jijuntun Group (E_2j), and coal of Guchengzi Group (E_2g). Moreover, the green mudstone (E_2x) is interbedded with multiple thin layers of brown shale and light green marl, and is characterized by layer structure and fracture development. The green mudstone is widely exposed on the slope, accounting for 88% of the total slope surface with a thickness of 102 to 600 m and an average thickness of 421 m. The oil shale (E_2j) and coal (E_2g) are the main mining layers of the Fushun west opencast mine and are mainly distributed in the deep part of the north highwall. The oil shale (E_2j) is in conformity contact with the overlying green mudstone (E_2x) with an average thickness of 194 m. The thickness of the coal layer (E_2g) varies considerably between 30 and 120 m and is in conformity contact with the overlying oil shale (E_2j). The contact relationship between the formations of sand shale (K_2d) and granitic gneiss (Ar_3) is unconformity, and the sand shale (K_2d) is in fault contact with green mudstone (E_2x).

The orientation of the green mudstone is expressed as an average dip direction of 350° and a dip angle of 25°–55°. The orientations of oil shale (E_2j) and coal (E_2g) are consistent with the occurrence of the green mudstone (E_2x), and continue to be stable along the direction and tendency. The sand shale (K_2d) and granitic gneiss (Ar_3) have an average dip direction of 345–350° and a dip angle of 25°–55°. It is noted that the green mudstone (E_2x) in the landslide area is characterized by anti-dipped structure, which generally provides favorable conditions for slope stability. However, the rock mass in the landslide area is weathered by physical, chemical, and biological processes acting hundreds of years (weathering grades IV–VI according to the International Society of Rock Mechanics classification system (ISRM 1981)), and the structural geology of the rock mass has a little contribution to the slope stability. Besides, the weathered green mudstone is vulnerable to strength reduction when it encounters rainwater, but to make matters worse, no drainage measures such as drains and ditches were built behind the crest or on benches to intercept the water. These factors could provide favorable conditions for the formation of the landslide.

The landslide area is also characterized by a synclinal fold in the N75°E direction and two reverse faults (F_1 and F_{1A}) in the N70°–80E direction (Fig. 3). The F_1 fault is exposed at the crest of the north highwall with a dip direction of 330° to 350° and a dip angle of 47° to 52°, and the width of the fault fracture zone is about 10 m. The F_{1A} fault is about 200 m away from the landslide scarp, whose dip direction ranges from 330° to 350° and dip angle ranges from 78° to 80° with a fault fracture

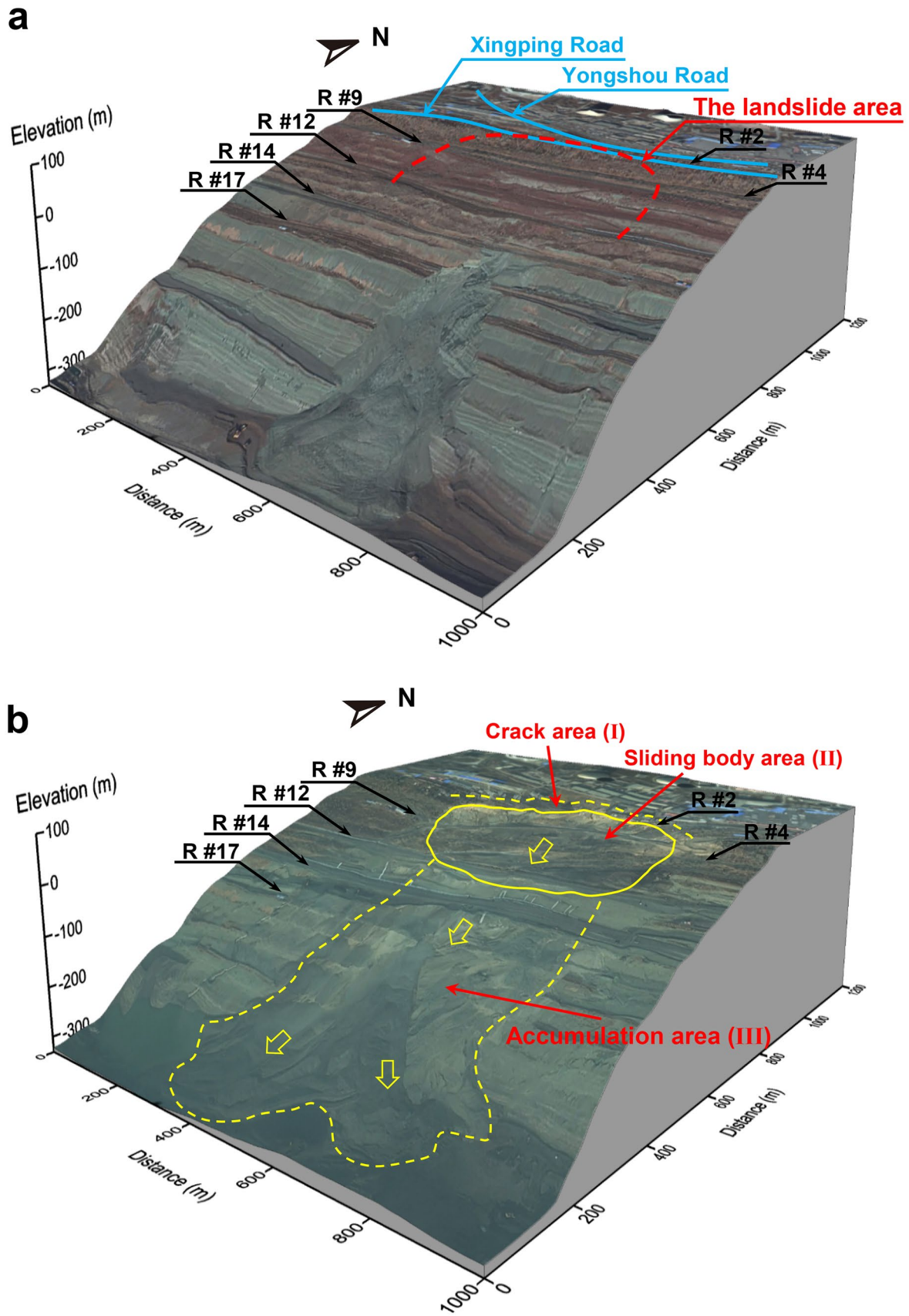

Fig. 4 Topography of the landslide area: **a** pre-sliding topography obtained from measured data in May 2016, **b** post-sliding topography obtained from measured data in September 2016

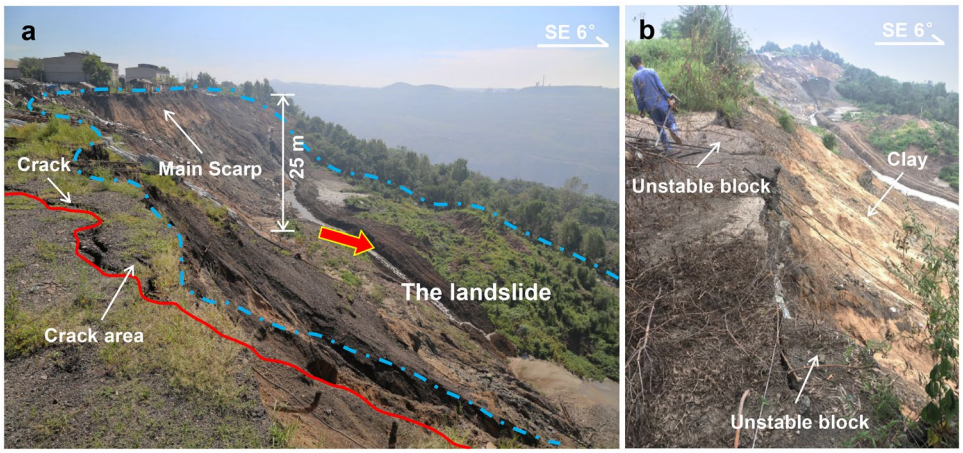

Fig. 5 The crack area (I) at the top of the landslide: **a** main scarp of the crack area, **b** unstable blocks of the crack area

zone of 80 m wide. Although both the F_1 and F_{1A} faults are adversely orientated faults, there are many weak fractures developed in the rock mass near the fault zone due to tectonic action. These structural features damaged the integrity of the rock mass, forming an effective infiltration channel for rainwater, which could also provide favorable conditions for the landslide occurrence (Li et al. 2015; Fan et al. 2017).

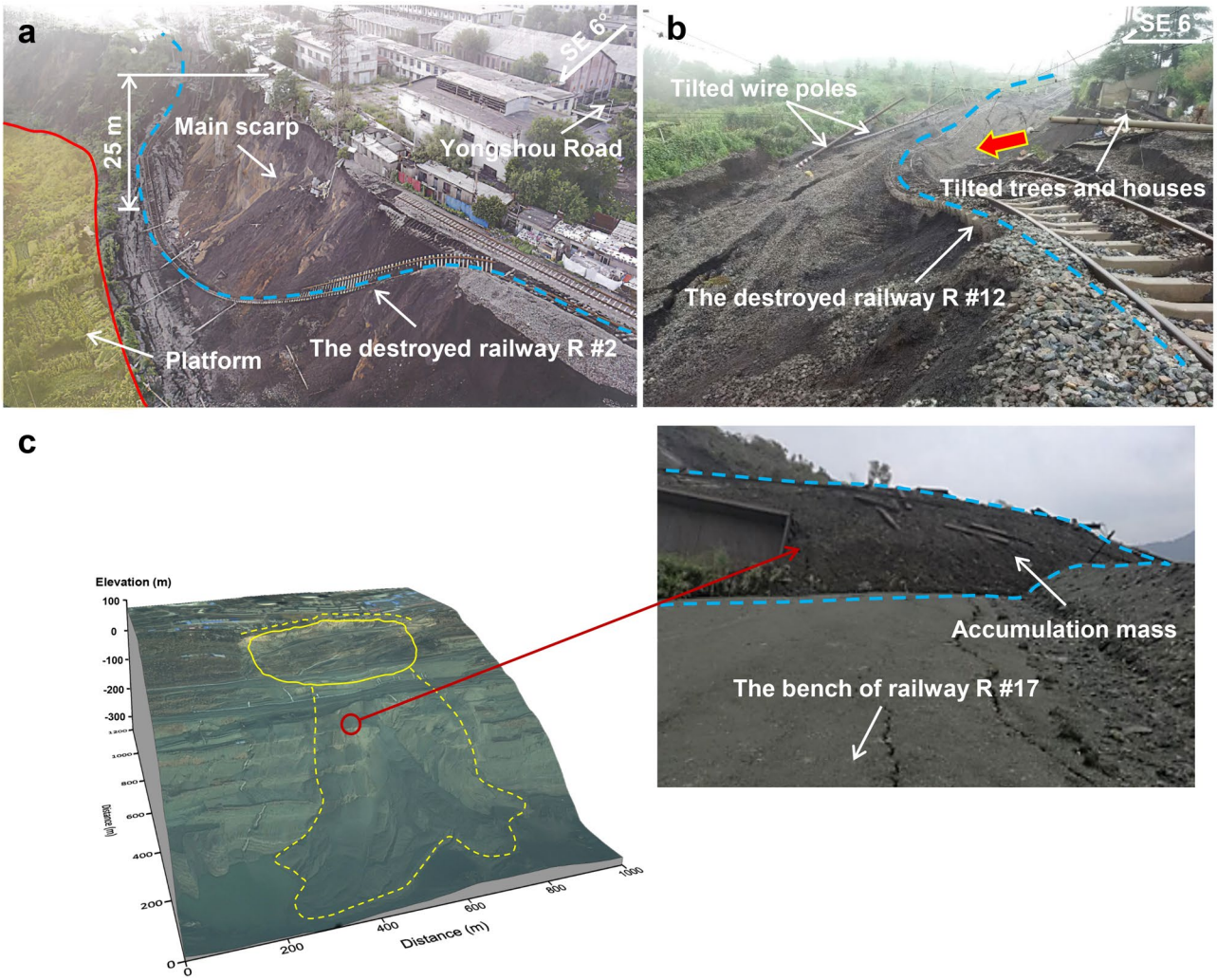

Fig. 6 The sliding body area (II) and the accumulation area (III): **a** rear part of the sliding body, **b** front part of the sliding body, **c** accumulation mass on the slope benches

Hydrogeological conditions of the landslide area

In the landslide area, the groundwater is mainly bedrock fissure water, and the aquifer is mainly the weathered green mudstone. The aquifer is mostly recharged by Hun river and rainfall. The Hun river is located in the north of the open pit, at a distance of 1.5 km from the landslide area (Fig. 2). The average water level of the Hun river is 70 m a.s.l., and the continuous infiltration of river water forms groundwater seepage in the bedrock fissures of the study area. The groundwater level (GWL) of a typical wet season is shown as a dashed blue line in Fig. 3, which ranges from 5 to 20 m below the ground surface and fluctuates in different seasons. Herein, GWL data are obtained in July 2015 from the four hydrological observation boreholes (B01, B02, B03, and B04) instrumented by piezometers, which are maintained by the Fushun Mining Group Co., Ltd. (FMGL); these piezometers record groundwater pressure every 2 h, which is then converted into groundwater levels. Following Li and Wang's (2015) report, FMGL installed the four piezometers; three of them had distorted data due to aging and disrepair in 2015 and therefore unable to record further groundwater pressure. The monitoring data from 2010 to 2015 demonstrated that the annual fluctuation of the GWL during the same dry and wet seasons was less than a few feet or a meter. The effect of such change has a minimum effect on the GWL variation within the slope, as indicated in the recorded data from January 2014 to December 2016 of borehole B04, which is still in use, shown in Fig. 7a. Besides, in the field survey, we found that groundwater outcropping points were widely distributed on the slope surface with elevations below − 32.5 m, which approximately confirms elevation of the outlet location of the GWL. Under the influence of long-term erosion by groundwater, the strength of

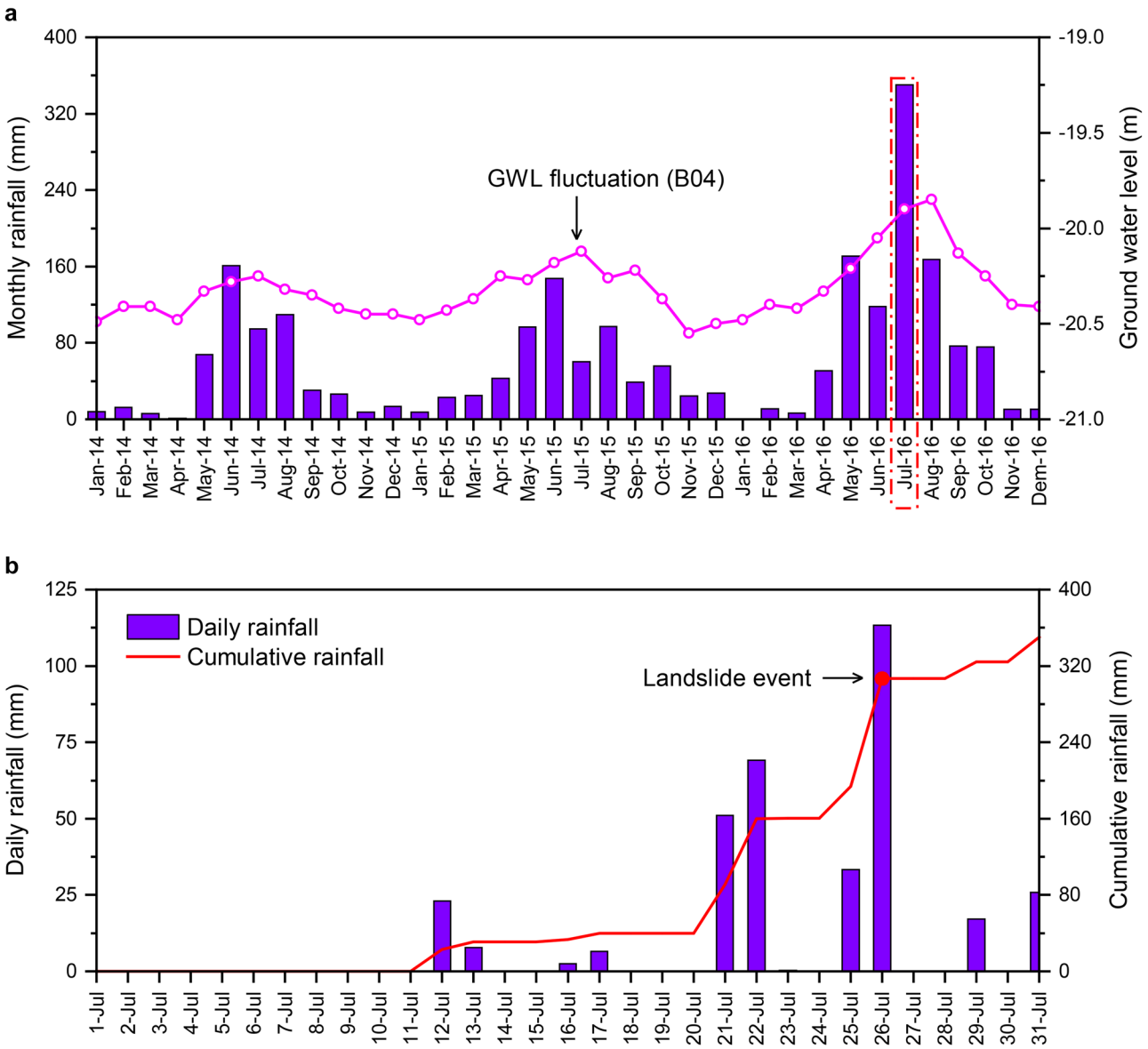

Fig. 7 Measured rainfall data and groundwater level of borehole (B04)

green mudstone below the GWL decreased continuously. This effect has a significant impact on the stability of the slope.

The rainfall is characterized by high intensity and concentration in Fushun region, and the historical (between 2010 and 2015) maximum intensity of rainfall of 77.2 mm/h was recorded on August 16, 2013 (He and Chen 2016). According to the rainfall data recorded by the station (no. 54351) within 1.5-km radius from the landslide site, the rainfall was relatively frequent and high intensity in July 2016 (Fig. 7a). Rainfall occurred on 13 of the 31 days of the month, with a total rainfall of 350 mm, which was notably higher than that during the same period in previous years. It is noted that the landslide area experienced heavy rainfall before the event, and daily rainfall on July 26 was 113.3 mm (Fig. 7b). Many researchers (e.g., Corominas 2001; Chowdhury et al. 2010) have demonstrated that shallow debris flows are often triggered by intense rainstorms of short duration, whereas deep-seated landslides are triggered by antecedent rainfall (high cumulative rainfall) over days or weeks often combined with intense rainfall over a much shorter period (an exceptional rainfall event). Based on the rainfall patterns before the occurrence of the landslide event, we concluded that the antecedent long-term rainfall decreased the stability of the slope, and the high-intensity rainfall on July 26, 2016, triggered the landslide event.

Mineral composition and microstructure of the green mudstone

Since the landslide mainly occurred on the upper green mudstone, the characteristics of the green mudstone have a great influence on the occurrence of the landslide. We conducted X-ray diffraction (XRD) and scanning electron microscope (SEM) observations on the green mudstone so that we could obtain some findings of the mineral composition and microstructure of the green mudstone. XRD analysis revealed that the green mudstone is composed mainly of muscovite, feldspar, and analcime, with some minor partings of montmorillonite and quartz. The content of muscovite and feldspar is high, which is 44% and 22%, respectively. It is also noted that the content of montmorillonite in the sample is 12% of the entire mineral composition, which is a hydrophilic expansive mineral contributing to the expansive behavior of the green mudstone. According to China Standard for Identification and Description of Rock and Rock mass (China Association for Engineering Construction Standardization 2008) and the American Standard Test Method for Expansion Index of Soils (American Society for Testing and Materials 2011), the green mudstone belongs to the micro-expansive rock. From the SEM images (Fig. 8), we can see that relatively large pores and fractures are common features in the green mudstone. Since the expansive rock is called shrink-swell rock (Miao et al. 2002; Stoltz et al. 2012), the fractures may result from this behavior.

Formation mechanism of the landslide

Based on field investigation and comprehensive analysis above, a conceptual model of the landslide mechanism was constructed as shown in Fig. 9. The formation process of the landslide can be divided into four stages:

1. Unloading and cracking stage (Fig. 9a), which is the first stage of the landslide: In this stage, the free face formed by the excavation was in an unloading state, and the elastic strain energy had been accumulated in the slope. Under the action of gravity, the geotechnical material gradually yielded and deformed, and a series of tension cracks gradually formed on the crest of the slope.
2. Sliding and partial locking stage (Fig. 9b), which is the second stage of the landslide: In this stage, due to the action of rainwater, a potential sliding surface was gradually formed by the relative shear deformation of the weakened rock mass. Because there was a significant resisting effect in the front rock mass due to its higher strength, the whole landslide mass failed to cut through the face, thus caused the partial locking at the toe of the landslide (Sun et al. 2021).
3. Shearing out and failure stage (Fig. 9c), which is the third stage of the landslide: In this stage, the significant shear deformation occurred in the sliding zone, while the sliding body kept relatively good integrity and showed rotational sliding. With the high-intensity rainfall triggering the failure, the elastic strain energy accumulated in the slope was released rapidly, which caused the shearing out of the leading edge of the slide. Meanwhile, the main scarp on the top of the slope was developed and dragged the rear body, and a platform was formed at the rear of the slide.
4. Flowing and accumulating stage (Fig. 9d), which is the last stage of the landslide: In this stage, due to the pushing action of the sliding body, some rock debris collapsed and accumulated on the slope benches, while others were continued to fall down and deposited at the bottom of the pit thus formed areas of accumulation. The entire landslide process was completed.

Based on field observations and the analysis of landslide deformation and failure, the factors that caused the landslide are outlined below:

(a) Mining activities: The main engineering activity in this area was open mining, which resulted in an open pit with a depth of about 400 m. We found that the north highwall was disturbed by long-term excavation, unloading, and blasting vibration. Therefore, the landslide was closely linked with mining activities.

(b) The weak rock mass: The green mudstone contained minerals of muscovite, feldspar, analcime, montmorillonite, and quartz, which is a typical weak rock. Furthermore, many relatively large pores and fractures developed in the green mudstone, which may play an important role in rainfall water entering into the slope. This effect has a significant impact on the stability of slopes.

(c) Unfavorable geological structure: The F1 fault and its associated faults pass through the rear edge of the landslide area, which provided a separation face for the rear edge of the landslide. These faults destroyed the integrity of the slope and formed a favorable condition for cracks. The well-developed cracks provided an effective infiltration channel for rainwater and the appropriate geological promise for the occurrence of the landslide.

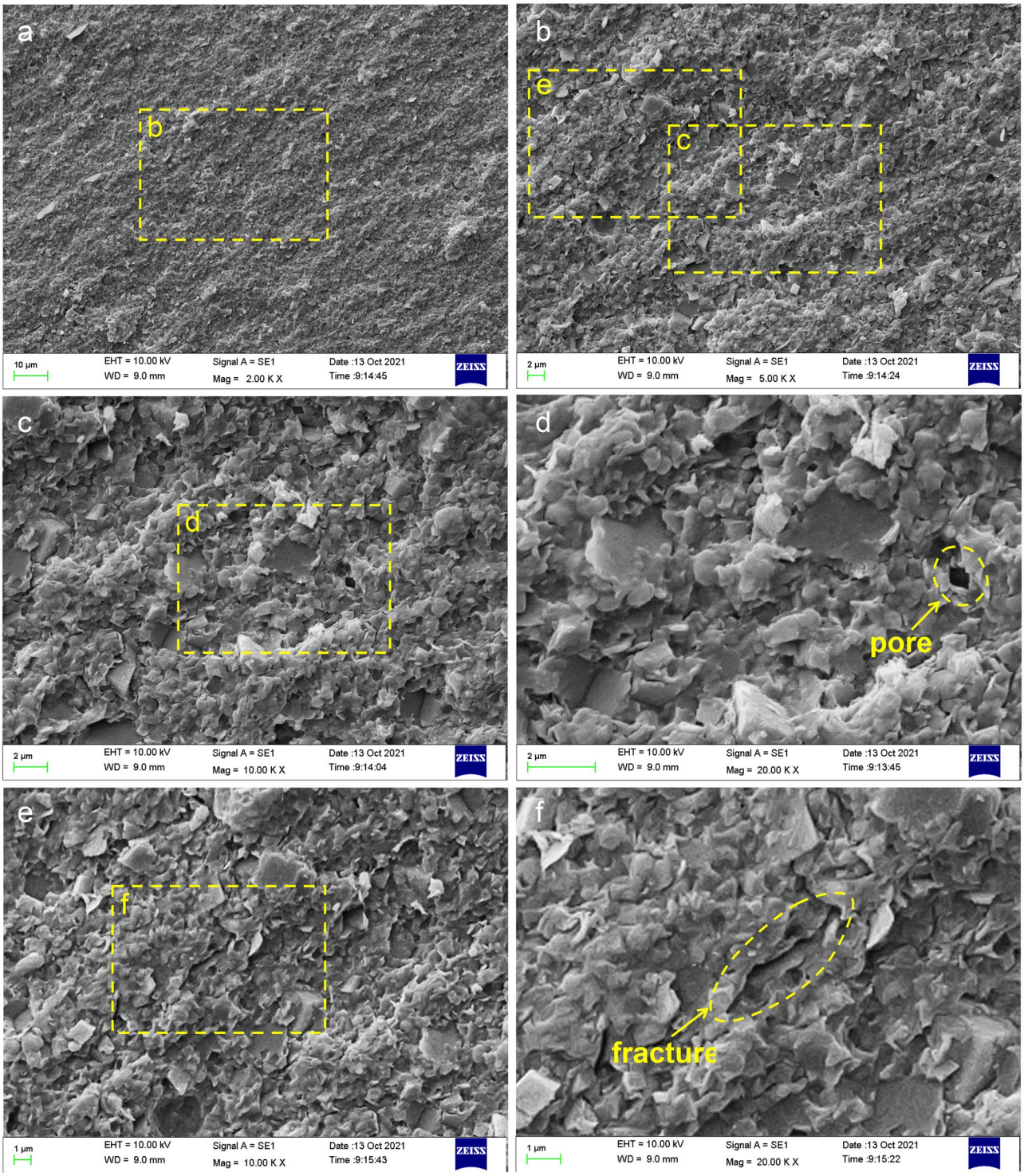

Fig. 8 Microstructure characteristics of intact green mudstone: **a**×2000 times, **b**×5000 times, **c**×10,000 times, **d**×20,000 times, **e**×10,000 times, **f**×20,000 times

(d) Heavy rainfall: The large amounts of accumulated rainfall combined with high rainfall intensity were the most important factor causing the landslide. According to the local rainfall data in July 2016, rainfall reached 350 mm in the landslide area, which was significantly higher than the same period in the previous years. The heavy rainfall infiltration increased the saturation of the rock mass and caused an increase in pore pressure in the slope. Furthermore, the rock-water interaction deteriorated the shear strength of the rock mass.

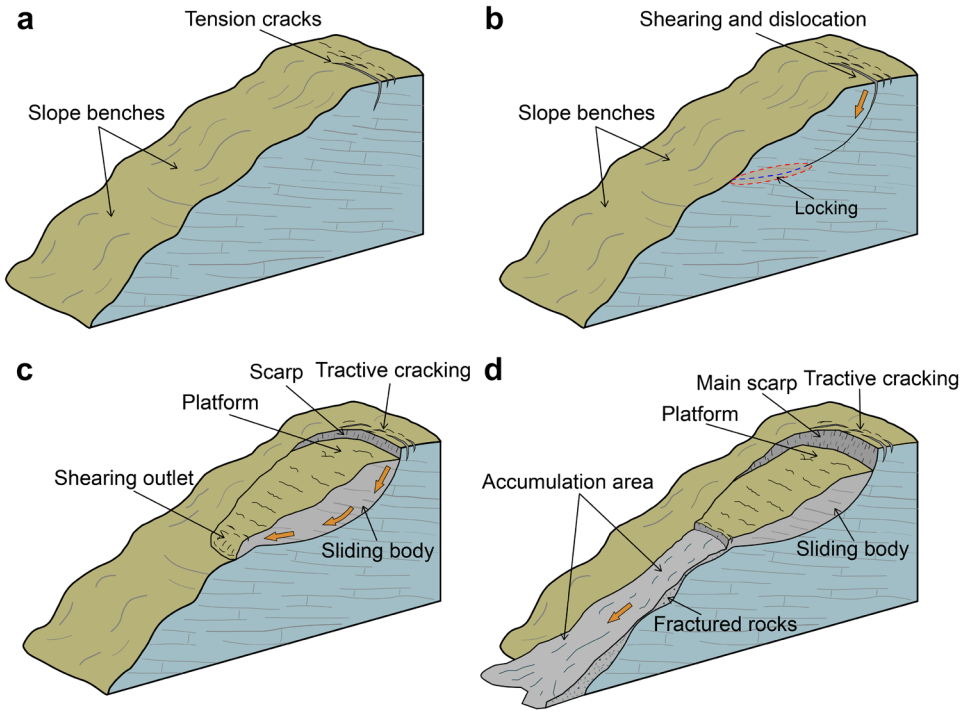

Fig. 9 Conceptual model of the formation mechanism of the landslide: **a** unloading and cracking stage, **b** sliding and partial locking stage, **c** shearing out and failure stage, **d** flowing and accumulating stage

Numerical simulation of the landslide

Considering the fully coupled hydromechanical analysis is complex and time-consuming, a simplified coupled seepage and stability analysis was performed to explore the landslide mechanism. In this analysis, the pore-water pressures obtained from the transient seepage analysis developed in the context of unsaturated soil mechanics were included in the limit equilibrium analysis to assess the effect of rainfall infiltration on slope stability. The computational work presented here was carried out using the Geostudio 2018 developed by GEO-SLOPE International Limited (2018a). GeoStudio is a two-dimensional commercial code for geotechnical analysis that has the ability to simulate the pore-water pressure distributions in a slope subjected to rainfall, and the obtained results can subsequently be coupled with stability analysis to determine how the transient rainfall infiltration affects a slope over time (Raj and Sengupta 2014; Peranić et al. 2021).

Material properties

The properties needed for the analysis are categorized into three groups, physical, strength, and hydromechanical, as shown in Table 1. The laboratory test indicated that the highly weathered green mudstone has a specific gravity of 2.7, a porosity of 0.3, a natural volumetric water content of 0.11, and a unit weight of 19.58 kN/m^3. The plastic limit and liquid limit of mudstone samples were 9.6% and 42.3% by plasticity and cone penetrometer tests, respectively. The shear strength of the green mudstone was obtained from conventional drained direct shear tests following the China Standard for Test Methods of Engineering Rock Mass (National standard of the People's Republic of China 2013) and the American Society for Testing and Materials (American Society for Testing and Materials 2006). The tests show that the green mudstone has a cohesion (c') of 52 kPa and an effective internal angle of friction (φ') of 14.5°.

The relationship between water content and matric suction represented by the soil–water characteristic curve (SWCC) and the relationship between hydraulic conductivity and matric suction represented by the hydraulic conduction curve (HCC) are two important characteristic functions in the analysis of unsaturated slope infiltration (Fredlund and Rahardjo 1993). Many previous researchers have focused on water retention behavior under low matric suction with remolded samples due to the difficulty of on-site sampling. In this study, the undisturbed samples were collected according to the following steps: (i) remove 60-cm-thick topsoil on the surface of the landslide; (ii) place down the 61.8-mm diameter and 20-mm-high ring-knife with a thin layer of Vaseline coated on the inner wall on the exposed layer; (iii) press the ring-knife down vertically and cut down the surrounding part by a knife; and (iv) cut the remnants along the outer side of the ring-knife to smooth the upper and lower parts with a steel wire saw. The axis-translation technique was used to obtain the SWCC data. The instrument used for measuring the SWCC is the 1D-SDSWCC pressure plate instrument with 15 bar high air-entry ceramic disc produced by Geo-experts, UK. The prepared green mudstone sample was saturated initially and then placed on the ceramic plate in the pressure chamber with no vertical load, and

Table 1 Hydromechanical properties of site material

Material	γ (kN/m^3)	c' (kPa)	φ' (°)	k_s (m/s)	θ_r	θ_s	α	n
Highly weathered green mudstone	19.58	52	14.5	3.47e-6	0.07	0.3	2.5e-3	2.8

the air pressure was applied step by step to 1 MPa. The weight, diameter, and height of the sample were measured when the drainage and deformation reach equilibrium at each suction level. The changes in plate cell weight were used together with the final dry weight of the sample to back-calculate the water content of the sample that existed at each of the various applied pressures. In this manner, the volumetric water content versus matric suction relationship was developed as shown in Fig. 10a. The SWCC data obtained from the pressure plate tests were fitted to the Van Genuchten volumetric water content function Eq. (1) using the RETC code (Van Genuchten et al. 1991) as shown in Fig. 10a. The three main features that characterize the SWCC are the air-entry value, the slope of the function, and the residual water content. The air-entry value of the weathered green mudstone is about 105 kPa reflecting how much suction can be applied to the pore-water before the largest pores or voids start to drain. The residual water content represents the volumetric water content of a soil where a further increase in negative pore-water pressure does not produce significant changes in water content. Since the residual conditions were not achieved for the range of pressure considered, a value of 0.07 was specified as the residual water content based on the fitting curve in Fig. 10a and our understanding of field conditions. The saturated hydraulic conductivity was determined to be 3.47e-6 m/s following the Li and Wang's (2015) report using falling head permeability tests. Then, the hydraulic conduction curve (HCC) was estimated from the SWCC using the Van Genuchten hydraulic conductivity function Eq. (2) to improve the stability of numerical solutions (Vogel et al. 2001). The resulting curve is shown in Fig. 10b. The Van Genuchten model is considered to provide a better match to experimental data and its parameters have been accumulated for many types of geomaterials (Leong and Rahardjo 1997).

$$\theta_w = \theta_r + \frac{\theta_s - \theta_r}{\left\{1 + \left[\alpha\left(u_a - u_w\right)\right]^n\right\}^m} \tag{1}$$

$$k_w = k_s \frac{\left\{1 - \left(\alpha\left(u_a - u_w\right)\right)^{n-1}\left[1 + \left(\alpha\left(u_a - u_w\right)\right)^n\right]^{-m}\right\}^2}{\left[1 + \left(\alpha\left(u_a - u_w\right)\right)^n\right]^{\frac{m}{2}}} \tag{2}$$

where Θ_w is the volumetric water content; $(u_a - u_w)$ is the matric suction; Θ_r and Θ_s are the volumetric water contents at the residual and saturated states, respectively; α and n are curve fitting parameters as listed in Table 1, $m = 1 - 1/n$; k_w is the hydraulic conductivity at matric suction; and k_s is the saturated hydraulic conductivity.

Method of analysis

The slope was simplified as a plane problem to be modeled based on the geological section from Fig. 3. It is noted that the green mudstone (E_2x) in the upper part of the slope at which the landslide occurred is highly weathered, whereas the lower green mudstone (E_2x) and oil shale (E_2j) are moderately weathered or slightly weathered. For simplicity, the upper green mudstone was singled out for the model. Besides, the sand-shale layer (E_2d) was assumed to be the same as that of the upper green mudstone (E_2x). This choice was made due to the lack of testing data and likely has little influence on results given the fact that the failure is mainly within the green mudstone (E_2x). In this manner, we simplified the model as a single media between elevations − 100 m and + 75 m a.s.l. The model consisted of 500 m in length (x-direction) and 175 m in depth (z-direction) and was divided by 7705 elements and 7888 nodes (Fig. 11).

The coupled analysis in this study consists of two main parts: seepage analysis and slope stability analysis. In the seepage analysis, because there was no field measurement of pore pressure or water content, we applied a steady-state analysis to obtain the initial condition for the transient seepage analysis according to the

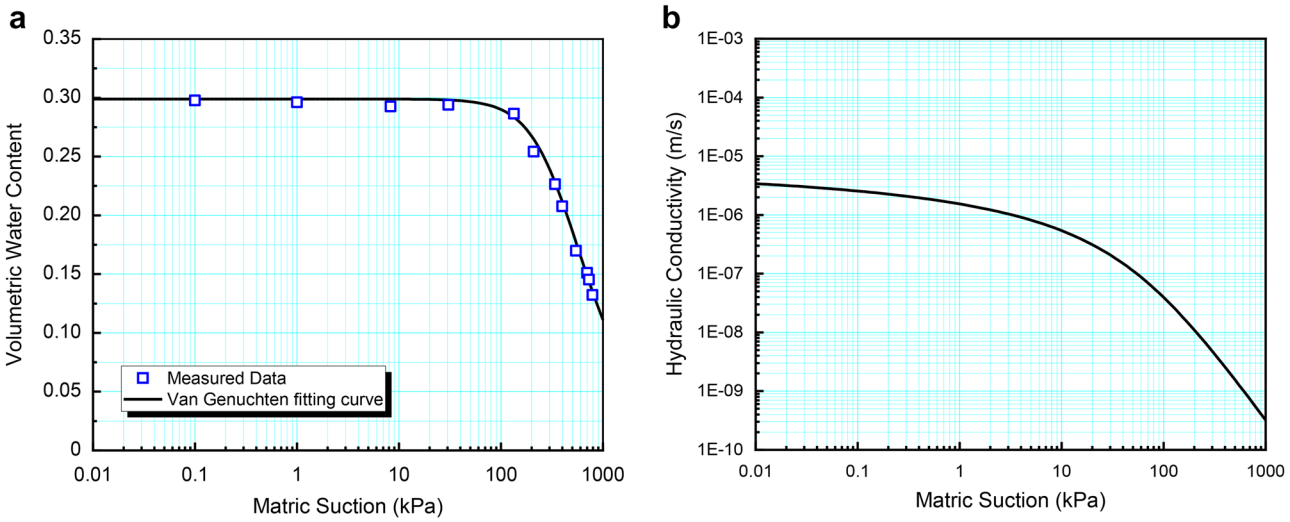

Fig. 10 Hydraulic properties of the green mudstone: **a** volumetric water content curve, **b** hydraulic conductivity curve

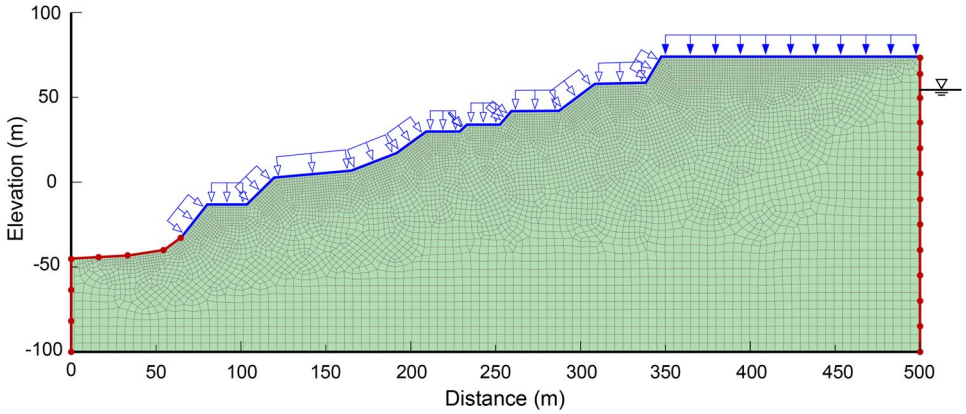

Fig. 11 Numerical model of the north highwall

GWL in Fig. 3. The right boundary condition was specified as a total head equal to the elevation of the groundwater table of 55 m (Fig. 11), which is often referred to as the far field boundary (GEO-SLOPE International Limited 2018a). Specifying a constant total head as a far field boundary condition implies that sufficient water is somehow going to come to that location so that the head remains a constant. Physically, this is acceptable as there is the Hun River up against the far field end of the problem, as shown in Fig. 2, and the river remains at a constant level depending on the season. For the slope surface with elevations below − 32.5 m (Fig. 11), the water table is at the ground surface; that is, the water pressure is zero at the slope surface and the total head is the elevation of the ground surface; therefore, a constant pressure boundary condition with zero pressure head was specified. Besides, the left boundary condition was specified as a total head equal to − 45 m with an underdrain condition, and the bottom was fixed zero flux. Then, transient seepage simulation was conducted to obtain the pore-water pressure distributions within the slope for given rainfall intensity and duration. Here, boundary conditions for the sides and bottom of the domain remain identical to the ones in the steady-state analysis, whereas the top boundary is set to possible seepage with a specified flux. Since little record on rainfall at the landslide area in terms of intensity and duration of the rainfall is available, nothing could be determined with confidence how much rainfall triggered the landslide. In order to investigate the rainfall thresholds for the landslide, we divided the amount of rainfall in an event by the total duration of the rainfall to narrow the window for the plausible infiltration rate and applied it at the slope boundary as a surface flux (Fig. 11). In this study, the rainfall intensities 4, 8, 16, 24, and 32 mm/h were considered, and the results were recorded at 2.4 h interval for 1 day. Both the steady-state and transient seepage analyses assume that the pore-air pressure equals the atmospheric pressure; thus, the change in volumetric water content depends only on the change in pore-water pressure.

The seepage analyses were performed using the SEEP/W module (GEO-SLOPE International Limited 2018a). The change in pore-water pressure during infiltration was analyzed. The equation governing the transient flow of water through unsaturated slopes is given as:

$$\frac{\partial}{\partial x}\left(k_x \frac{\partial H}{\partial x}\right) + \frac{\partial}{\partial y}\left(k_y \frac{\partial H}{\partial y}\right) + Q = m_w \rho_w g \frac{\partial H}{\partial t} = \frac{\partial \theta_w}{\partial t} \quad (3)$$

where the k_x is the hydraulic conductivity in x-direction; k_y is the hydraulic conductivity in y-direction; H is the hydraulic head; Q is the applied boundary flux; m_w is the water storage modulus obtained by differentiating the SWCC; and ρ_w is the water density. The equation shows that the variation of water stored within the slope depends on the fluxes entering and leaving the elemental volume. More fundamentally, it illustrates that the sum of the rates of change of flows in the x and y directions plus the external applied flux is equal to the rate of change of the volumetric water content with respect to time.

The stability of the slope was analyzed by considering the pore-water pressure from the above seepage analysis using the SLOPE/W module (GEO-SLOPE International Limited 2018b). The SLOPE/W program considers unsaturated shear strength conditions when the matric suction exists or the pore-water pressure is negative. The shear strength of the soil is determined using Eq. (4). The equation can describe and predict the nonlinear relationship between matric suction and shear strength of the soil, which provides a better representation of unsaturated geomaterial behavior and is widely used to analyze the slope stability under rainfall conditions (Cai and Ugai 2004; Oh and Lu 2015; Peranić et al. 2021).

$$\tau = c' + (\sigma_n - u_a)\tan\varphi' + (u_a - u_w)\left[\left(\frac{\theta_w - \theta_r}{\theta_s - \theta_r}\right)\tan\varphi'\right] \quad (4)$$

where τ is the shear strength and $(\sigma_n - u_a)$ is the net normal stress on the failure plane.

The factor of safety (FS) is defined as the ratio of the shear resistance and the mobilized shear stress along the entire length of the slip surface as:

$$FS = \frac{\Sigma \tau_{si}}{\Sigma \tau_{mi}} \quad (5)$$

where τ_{si} and τ_{mi} are the shear strength and the mobilized shear stress of an arbitrary slice i, respectively. The FS of the slope in this study was calculated using the Morgenstern-Price method (Morgenstern and Price 1965).

Simulation results

The reduction of the matric suction and the response of the water table under rainfall conditions were obtained by transient

simulation. Figure 12 illustrates the pore-water pressure distribution in the initial condition and at the end of 4.8, 7.2, and 9.6 h for the case of 16 mm/h intensity of rainfall. It can be seen that in all rainfall stages, very rapid pore-water pressure response was observed with the rainwater infiltrated into the slope. Initially, the pore-water pressure above the water table was negative, with a maximum matric suction of 426.48 kPa regardless of rainfall (Fig. 12a). With continuous rainfall, the maximum matric suction gradually decreases (Fig. 12b–c). Meanwhile, the water content in the shallow layer of the slope increases rapidly and the pore-water pressure becomes positive, indicating that a saturated area had formed at the crest of the slope. At the end of 9.6 h rainfall (Fig. 12d), the saturated area further enlarged and extended to the groundwater table, and the maximum matric suction was decreased to 285.55 kPa. However, the pore-water pressure in the deep layer of the slope remained constant with a maximum value of 1471.0 kPa.

The maximum matric suctions within the slope for each rainfall intensities and durations are compared in Fig. 13. It can be seen that the maximum matric suction decreases continually with the increase of rainfall intensity and duration. However, the significant matric suction remained in the slope even after 24 h of rainfall at lower intensities of 4, 8, and 16 mm/h. For the case of higher rainfall intensities of 24 mm/h and 32 mm/h, the matric suction disappeared after 21.6 and 16.8 h, respectively, which indicates that the slope was completely saturated. Numerous studies show the considerable effect of matric suction pressure on the stability of the slope, and the slope may become potentially unstable with the reduction of matric suction (Lu et al. 2013; Chen et al. 2020). During the time of rainwater infiltration, matric suction in the slope decreases, and thus, the effective shear strength of the slope reduces, which in turn may reduce the *FS* of the slope.

The *FS* of the slope for different rainfall intensities and duration are compared in Fig. 14, and all *FS* values were calculated using the one slip surface presented in Fig. 15a. For the initial condition, that is no rainfall, the calculated *FS* is 1.15. Note that a *FS* of 1.2 was selected as the minimum adequate value following the Chinese standard GB 51289–2018 (National Standard of the People's Republic of China 2018). Due to the occurrence of previous landslides and the deformation of the area, the slightly lower *FS* value is considered to be consistent with the actual conditions. For 4 mm/h rainfall, the *FS* remains above 1.0, indicating that the slope remains stable even after 24 h of rainfall. For 8 mm/h rainfall, the slope remains stable when the duration of rainfall is 12 h. Beyond 12 h of rainfall, its *FS* drops drastically. Similarly, for 16 mm/h and 24 mm/h rainfall, the slope remains stable only if the duration of the rainfall is within 7.2 h and 4.8 h, respectively. For 32 mm/h rainfall, the slope satisfies stability criteria when the duration of rainfall is 2.4 h, whereas the *FS* drops rapidly when the duration of rainfall exceeds 2.4 h. It should be noted that the *FS* decreases gradually at the stable stage and decreases sharply at the unstable stage. This difference is very likely due to the different actions of rainwater, and at the stable stage, the decrease of the *FS* was caused by the propagation of the wetting front, while at the unstable stage, the decrease of the *FS* could be attributed to the enlargement of the saturated area in the slope. The stability results indicate that if the rainfall intensity is more than 16 mm/h, the north highwall will not be stable after 7.2 h. As discussed before, this much of rainfall is usual for the Fushun region during the months of July and August. This possibly explains the destruction that occurred at the site after rainfall.

The critical failure surface obtained from the limit equilibrium analysis of the north highwall under rainfall conditions is shown in Fig. 15a. It can be seen that the critical failure surface matched the field surveys closely. SLOPE/W was able to read the seepage results directly from SEEP/W in order to compute the actual pore-water pressures at the base of each slice. Figure 15b shows the actual pore-water pressures applied on each slice for 16 mm/h rainfall with different durations. Note how the pore pressures on the slices change from negative to positive, as the slice number increases from left to right. It would not have been possible to accurately establish this type of pore-water pressure condition without the use of a rigorous saturated–unsaturated seepage flow model. Figure 15c illustrates the contributing strength components applied to the slope stability analysis for 16 mm/h rainfall after 2.4 h. The cohesion was fixed as a material property and is constant at 52 kPa. The frictional component depends on the slide base normal force and the suction component depends on the pore-water pressure as it varies across the slope. It is interesting to note the suction strength contribution and compare it with the seepage pore-water pressures. There is no suction strength where the pore-water pressures are positive. From the above analysis, we can conclude that the original slope was stable with a *FS* above 1.0 without considering rainfall, but unfortunately encountered July 26, 2016, heavy rainfall and caused the landslide. The development of pore-water pressure due to the decrease in matric suction and the decrease in shear strength of the green mudstone was the main mechanism that triggered the landslide.

It should be noted that the results presented in this study are based on two-dimensional simplified coupled seepage and stability analysis. However, the *FS* obtained by real three-dimensional analyses may be slightly higher than that obtained by plane problem analyses, and the difference was attributed to the three-dimensional effect of the landslide (Deng et al. 2007; Sun et al. 2021). An important limitation is also the fact that the unsaturated soil characteristic functions were derived from measurements made on the drying path, whereas the study analyzes the conditions experienced by the slope on the wetting path. Furthermore, there are several hydrological parameters such as evaporation, evapotranspiration, vegetative cover, depression storage, and surface runoff that can also affect the pore-water pressure distribution and overall stability of the slope, and the contributions of these factors on the occurrence of landslide require further research.

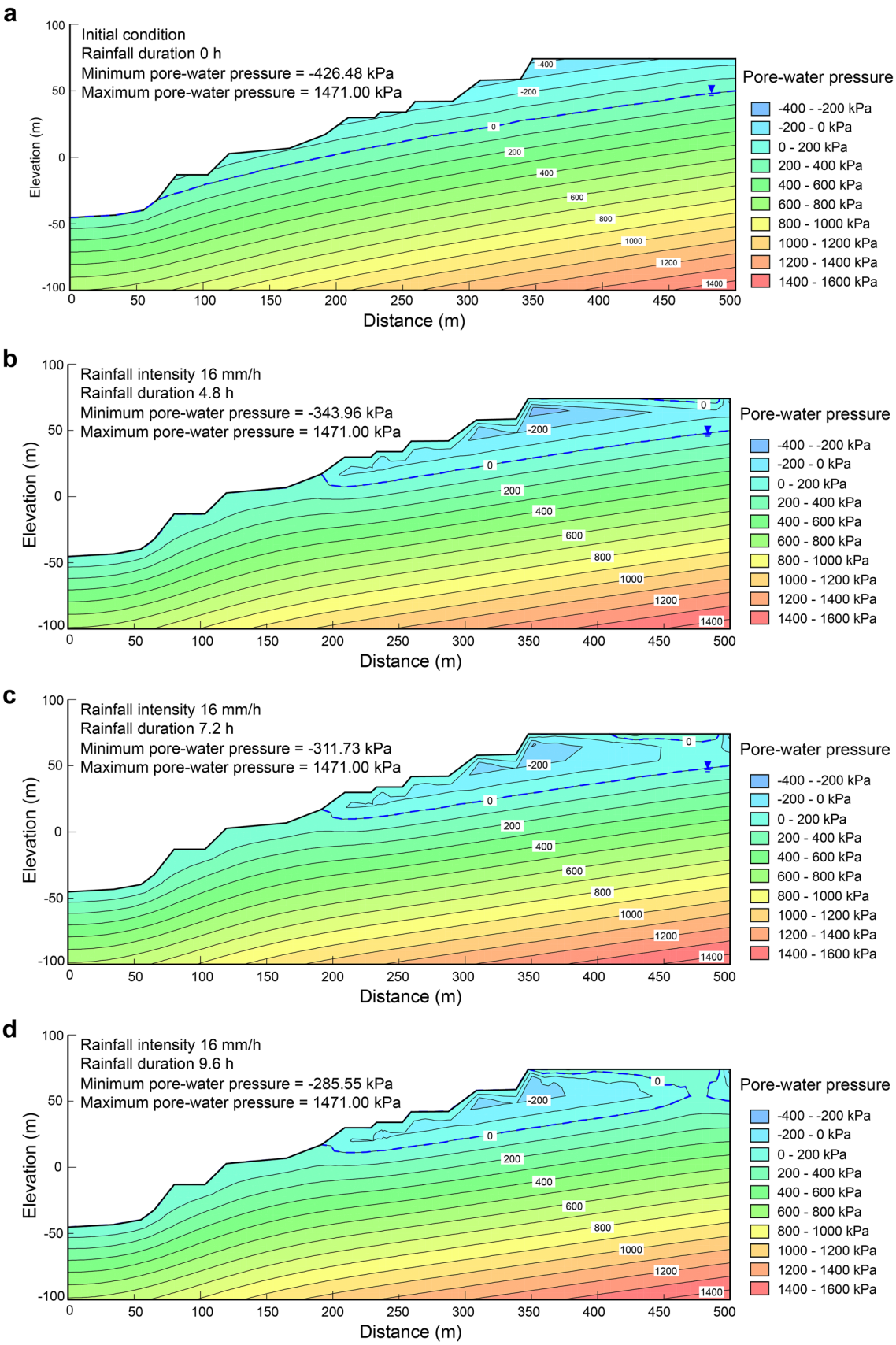

Fig. 12 Distribution of matric suction and pore-water pressure for 16 mm/h rainfall after **a** 0 h, **b** 4.8 h, **c** 7.2 h, and **d** 9.6 h

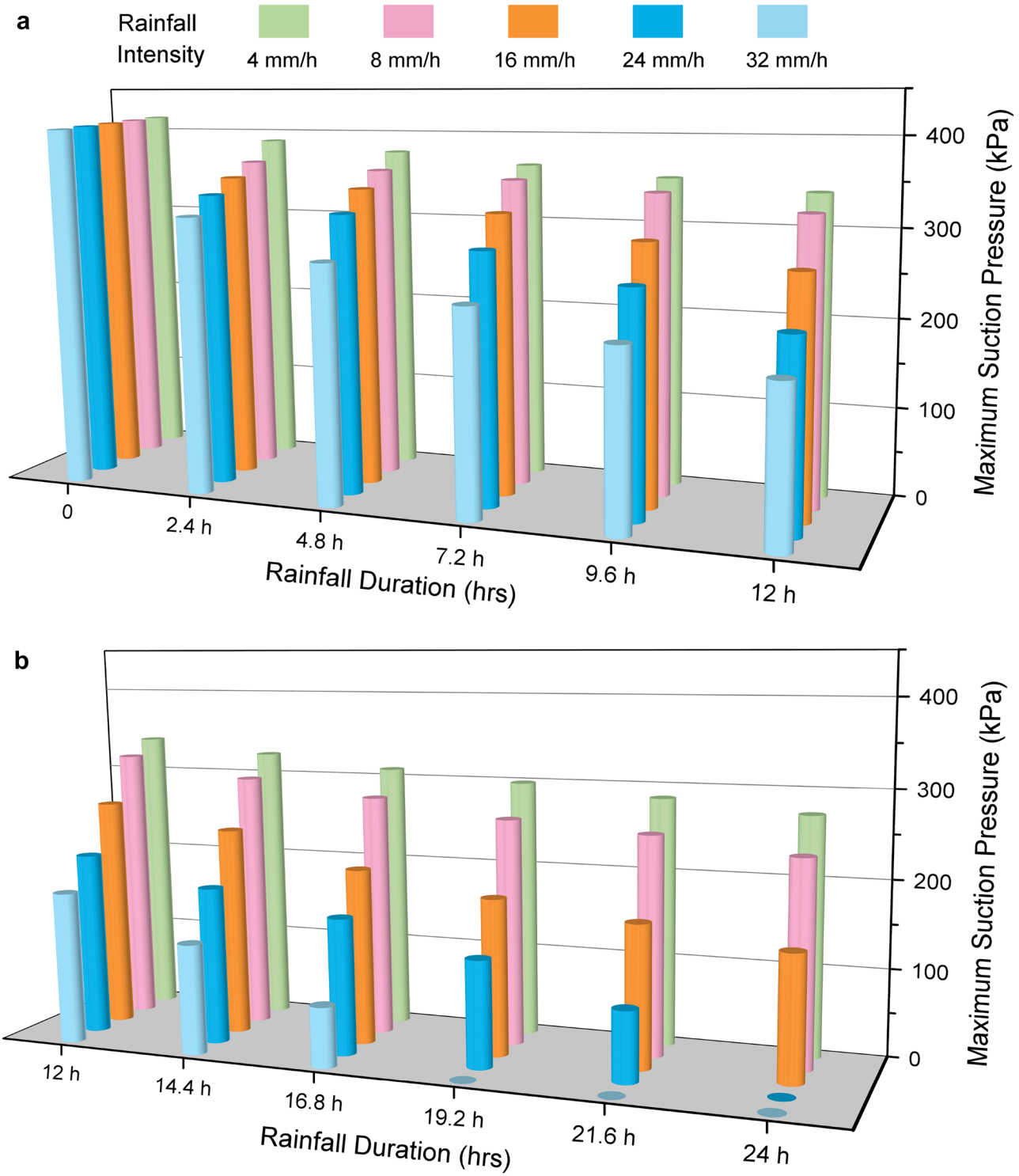

Fig. 13 Comparison of maximum matric suction within the slope with different rainfall intensities at the duration of **a** 0–12 h and **b** 12–24 h

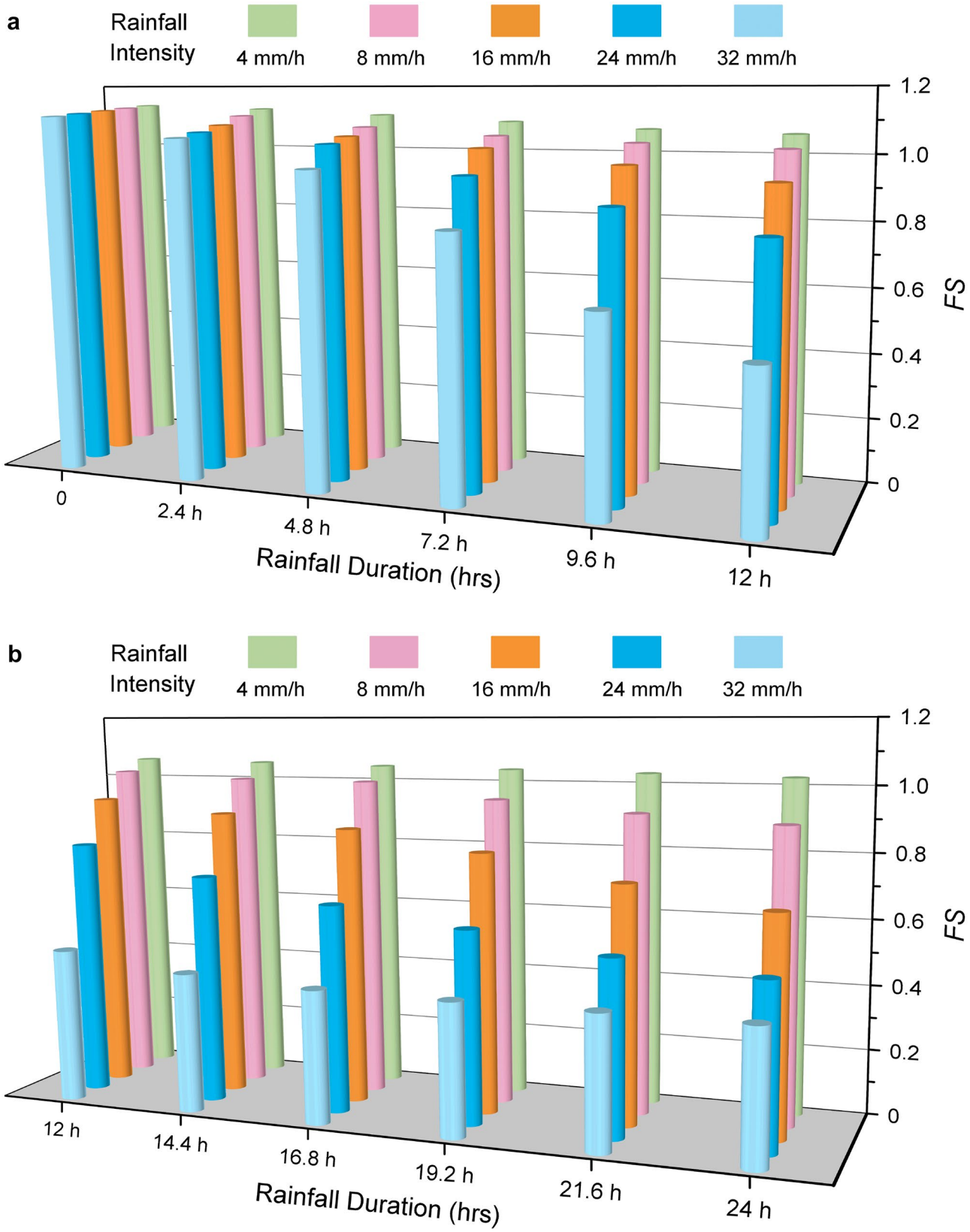

Fig. 14 Reduction of the factor of safety of the slope with different rainfall intensities at the duration of **a** 0–12 h and **b** 12–24 h

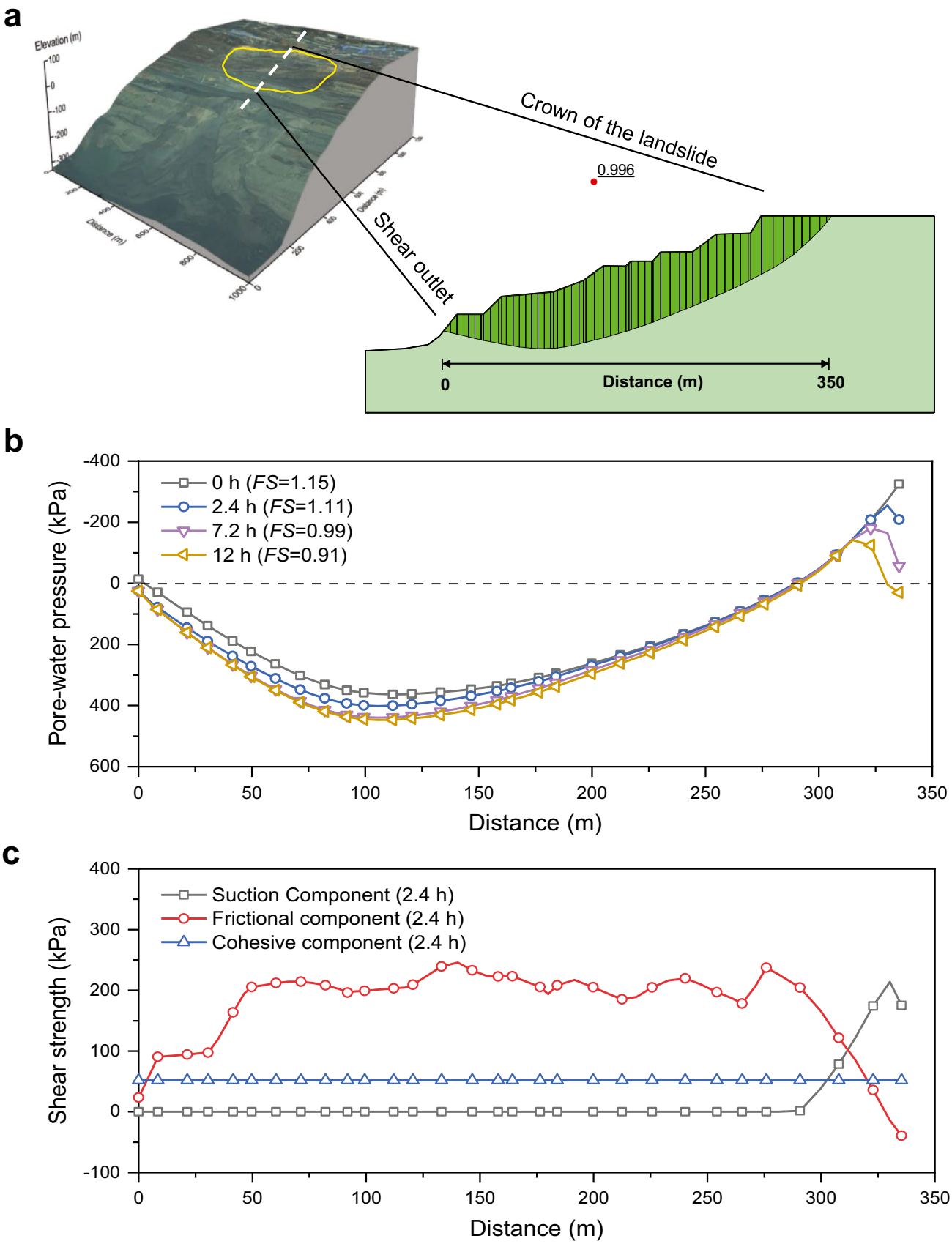

Fig. 15 The critical failure surface for 16 mm/h rainfall: **a** compare with the in situ investigation, **b** pore-water pressure changes with different durations, and **c** shear strength components at 2.4-h duration

Conclusions

A landslide occurred at 5:00 (UTC + 8) on July 26, 2016, in the north highwall of Fushun west open-pit, China, after the high-intensity rainfall. The failure characteristics of the landslide were summarized and the failure mechanism was analyzed. The following conclusions can be drawn from the study:

According to the field investigation, the landslide area was divided into three parts: the crack area, the sliding body area, and the accumulation area. The crack area was mainly formed by traction unloading of the landslide. The sliding body area is characterized by an arc-shaped sliding surface, slow or moderate velocities, and limited internal deformation. The accumulation area consists mainly of broken green mudstone with unclear edges and corners from the disintegration and fragmentation of the upper rock mass.

Taking the microscale of geotechnical properties into consideration, the mineral composition and microstructure of the green mudstone were obtained by using the X-ray diffraction and scanning electron microscope techniques. The green mudstone contained minerals of muscovite, feldspar, analcime, montmorillonite, and quartz and was identified as a micro-expansive rock. Relatively large pore and fracture are both very common features in the green mudstone, which could play an important role in the infiltration of rainwater into the slope and improving the permeability of the rock mass of the slope.

Based on field investigation and comprehensive analysis, a conceptual model of the landslide mechanism was constructed. The formation process of the landslide was divided into four stages: unloading and cracking stage, sliding and partial locking stage, shearing out and failure stage, and flowing and accumulating stage.

A simplified coupled seepage and stability analysis was performed to explore the mechanism of the landslide by numerical simulation using the Geostudio program. The relationship of volumetric water content and hydraulic conductivity to matric suction was established to describe the hydraulic characteristics of the slope material under infiltration. The seepage analyses were carried out using the SEEP/W module, while the stability of slope was analyzed using the SLOPE/W module based on the obtained pore-water pressure by the seepage analysis. The results show that the maximum matric suction in the slope decreases continually with the increase of rainfall intensity and duration, and the north highwall will not be stable after 7.2 h for 16 mm/h of rainfall intensity. It is indicated that the original slope was stable and heavy rainfall triggered the landslide; meanwhile, the critical failure surface obtained by a combined analysis plot matched closely the field surveys. The findings of the present case study successfully highlight the importance of considering these hydrogeological features in investigating the mechanism of rainfall-induced landslides.

Acknowledgements

This work was supported by the National Key Research and Development Plan (No. 2017YFC1503103) and the National Natural Science Fund of China (No. 51574245) and the Fundamental Research Funds for the Central Universities (2021YJSNY16). We would like to express our gratitude to the editors and reviewers for their constructive and helpful comments.

Author contribution

All authors contributed to this study. Shu-wei Sun designed the research study. Shu-wei Sun and Liu Liu analyzed the field data. Shu-wei Sun and Liu Liu wrote this paper. Jia-bing Hu and Hui Ding reviewed the manuscript. All authors gave final approval for publication.

Funding

Shu-wei Sun was supported by the National Key Research and Development Plan (no. 2017YFC1503103) and the National Natural Science Fund of China (no. 51574245) and the Fundamental Research Funds for the Central Universities (2021YJSNY16).

Availability of data and material

All data and material used to support the findings of this study are included in the article.

Code accessibility

All codes used to support the findings of this study are included in the article.

Declarations

Conflict of interest The authors declare no competing interests.

References

American Society for Testing and Materials (2006) Standard practice for classification of soils for engineering purposes (ASTM D2487–06 2006). Annual Book of ASTM Standards, West Conshohocken

American Society for Testing and Materials (2011) Standard test method for expansion index of soils (ASTM D4829–21). Annual Book of ASTM Standards, West Conshohocken

Cai F, Ugai K (2004) Numerical analysis of rainfall effects on slope stability. Int J Geomech 4(2):69–78

Chen XY, Zhang LL, Zhang LM, Zhou YD, Ye GL, Guo N (2021) Modelling rainfall-induced landslides from initiation of instability to post-failure. Comput Geotech 129:103877

Chen YL, Liu GY, Li N, Du X, Wang SR, Azzam R (2020) Stability evaluation of slope subjected to seismic effect combined with consequent rainfall. Eng Geol 266:105461

China Association for Engineering Construction Standardization (2008) Standard for identification and description of rock and rock mass (CECS239:2008). China Planning Press, Beijing (in Chinese)

Chowdhury R, Flentje P, Bhattacharya G (2010) Geotechnical slope analysis. CRC, New York

Chung MC, Tan CH, Chen CH (2017) Local rainfall thresholds for forecasting landslide occurrence: Taipingshan landslide triggered by Typhoon Saola. Landslides 14(1):19–33

Corominas J (2001) Landslides and climate. In: Bromhead EN (ed) Keynote Lectures delivered at the 8th International Symposium on Landslides, Cardiff, June 2000

Cui Y (2018) Analysis on geological characteristics and mechanism of landslide in south slope of West Open-pit Mine in Fushun. Jilin University (in Chinese)

Deng JH, Tham LG, Lee CF, Yang ZY (2007) Three-dimensional stability evaluation of a preexisting landslide with multiple sliding directions by the strength-reduction technique. Can Geotech J 44(3):343–354

Fan XM, Xu Q, Scaringi G, Dai LX et al (2017) Failure mechanism and kinematics of the deadly June 24th 2017 Xinmo landslide, Maoxian, Sichuan, China. Landslides 14:2129–2146
Fredlund DG, Rahardjo H (1993) Soil mechanics for unsaturated soils. John Wiley, New York
Gao B (2017) North slope landslide analysis and control research in Fushun West Open-pit Mine. Opencast Mining Technology 32(9):14–20 (in Chinese)
GEO-SLOPE International Limited (2018a) Seepage modeling with SEEP/W2018a version. GEO-SLOPE International Limited, Calgary, Alta
GEO-SLOPE International Limited (2018b) Slope modeling with SLOPE/W2018b version. GEO-SLOPE International Limited, Calgary, Alta
He H, Chen QL (2016) Diagnostic analysis and filtering comparison of heavy rainfall in Fushun area on August 16, 2013. J Chengdu Univ Inform Technol 31:30–36 (in Chinese)
Hungr O, Leroueil S, Picarelli L (2014) The Varnes classification of landslide types, an update. Landslides 11(2):167–194
International Society for Rock Mechanics ISRM (1981) Rock characterization, testing and monitoring. Pergamon Press, Oxford, ISRM suggested method
Jemec Auflič M, Jež J, Popit T et al (2017) The variety of landslide forms in Slovenia and its immediate NW surroundings. Landslides 14(4):1537–1546
Leong E, Rahardjo H (1997) Review of soil water characteristic curve equations. J Geotech Geoenviron Eng 123(12):1106–1117
Leshchinsky B, Vahedifard F, Koo HB, Kim SH (2015) Yumokjeong landslide: an investigation of progressive failure of a hillslope using the finite element method. Landslides 12(5):997–1005
Li Z, Wang JA, Li L, Wang LX, Liang RY (2015) A case study integrating numerical simulation and GB-InSAR monitoring to analyze flexural toppling of an anti-dip slope in Fushun open pit. Eng Geol 197:20–32
Li CH, Wang ZZ (2015) Feasibility report on comprehensive management of geological hazards in Fushun west open pit mine. Fushun Mining Group Co., Ltd
Lu N, Wayllace A, Oh S (2013) Infiltration-induced seasonally reactivated instability of a highway embankment near the Eisenhower Tunnel, Colorado, USA. Eng Geol 162:22–32
Miao LC, Liu SY, Lai YM (2002) Research of soil-water characteristics and shear strength features of Nanyang expansive soil. Eng Geol 65(4):261–267
Morgenstern NR, Price VE (1965) The analysis of the stability of general slip surfaces. Géotechnique 15(1):79–93
National Standard of the People's Republic of China (2018) Standard for design of slope engineering of open pit mine of coal industry (GB 51289–2018). China Planning Press, Beijing (in Chinese)
National Standard of the People's Republic of China (2013) Standard for test methods of engineering rock mass (GB/T 50266–2013). China Planning Press, Beijing (in Chinese)
Nguyen LC, Tien PV, Do TN (2020) Deep-seated rainfall-induced landslides on a new expressway: a case study in Vietnam. Landslides 17(2):395–407
Nie L, Li ZC, Zhang M, Xu LN (2015) Deformation characteristics and mechanism of the landslide in West Open-Pit Mine, Fushun. China Arab J Geosci 8(7):4457–4468
Oh S, Lu N (2015) Slope stability analysis under unsaturated conditions: case studies of rainfall-induced failure of cut slopes. Eng Geol 184:96–103
Ouyang C, Zhao W, Xu Q, Peng D et al (2018) Failure mechanisms and characteristics of the 2016 catastrophic rockslide at Su village, Lishui, China. Landslides 15:1391–1400
Peranić J, Mihalić Arbanas S, Arbanas Ž (2021) Importance of the unsaturated zone in landslide reactivation on flysch slopes: observations from Valići Landslide, Croatia. Landslides
Rahardjo H, Lim TT, Chang MF, Fredlund DG (1995) Shear strength characteristics of a residual soil. Can Geotech J 32(1):60–77
Raj M, Sengupta A (2014) Rain-triggered slope failure of the railway embankment at Malda. India Acta Geotech 9(5):789–798
Ren Y, Li TB, Dong SM, Tang JL, Xue DM (2020) Rainfall-induced reactivation mechanism of a landslide with multiple-soft layers. Landslides 17(5):1269–1281
Stoltz G, Cuisinier O, Masrouri F (2012) Multi-scale analysis of the swelling and shrinkage of a lime-treated expansive clayey soil. Appl Clay Sci 61:44–51
Sun SW, Pang B, Hu JB, Yang ZX, Zhong XY (2021) Characteristics and mechanism of a landslide at Anqian iron mine, China. Landslides 18(7):2593–2607
Van Genuchten MT, Leij FJ, Yates SR (1991) The RETC code for quantifying the hydraulic functions of unsaturated soils. U.S. Salinity Lab., Department of Agricultural Research Service, Riverside, CA
Vogel T, Van Genuchten MT, Cislerova M (2001) Effect of the shape of the soil hydraulic functions near saturation on variably-saturated flow predictions. Adv Water Resour 24(2):133–144
Wu LZ, Selvadurai APS, Zhang LM, Huang RQ, Huang JS (2016) Poromechanical coupling influences on potential for rainfall-induced shallow landslides in unsaturated soils. Adv Water Resour 98:114–121
Yang KH, Uzuoka R, Thuo JN, Lin GL, Nakai Y (2017) Coupled hydromechanical analysis of two unstable unsaturated slopes subject to rainfall infiltration. Eng Geol 216:13–30
Zhan JW, Wang Q, Zhang W, Shangguan YL, Song SY, Chen JP (2019) Soil-engineering properties and failure mechanisms of shallow landslides in soft-rock materials. CATENA 181:104093
Zhang G, Qian JY, Wang R, Zhang JM (2011) Centrifuge model test study of rainfall-induced deformation of cohesive soil slopes. Soils Found 51(2):297–305
Zhang CH, Zhang MS, Yu GQ (2016) Development and causes of group geological hazard in Tianshui City. Bull Soil Water Conserv 36(04):46–50+55 (in Chinese)

Shu-wei Sun · Liu Liu (✉) · Jia-bing Hu · Hui Ding
School of Energy and Mining Engineering, China University of Mining and Technology (Beijing), Beijing 100083, China
Email: liuliu_1280@163.com

Hui Ding
State Key Laboratory of Coal Mine Safety Technology, China Coal Technology & Engineering Group, Shenyang Research Institute, Fushun 113112, China